20th AIAA Aerodynamic Decelerator Systems Technology Conference and Seminar
4 - 7 May 2009, Seattle, Washington

AIAA 2009-2958

Optimal Control for Terminal Guidance of Autonomous Parafoils

Nathan J. Slegers*
University of Alabama, Huntsville, AL 35899-0266

Oleg A. Yakimenko†
Naval Postgraduate School, Monterey, CA 93943-5107

This paper deals with the development of guidance, navigation and control algorithms for a prototype of a miniature aerial delivery system capable of high-precision maneuvering and high touchdown accuracy. High accuracy enables use in precision troop resupply, sensor placement, urban warfare reconnaissance, and other similar operations. Specifically, this paper addresses the terminal phase, where uncertainties in winds cause most of the problems. The paper develops a six degree-of-freedom model to adequately address dynamics and kinematics of the prototype delivery system and then reduces it to a two degrees-of-freedom model to develop a model predictive control algorithm for reference trajectory tracking during all stages. Reference trajectories are developed in the inertial coordinate frame associated with the target. The reference trajectory during terminal guidance, just prior to impact, is especially important to the final accuracy of the system. This paper explores an approach for generating reference trajectories based on the inverse dynamics in the virtual domain. The method results in efficient solution of a two-point boundary-value problem onboard the aerial delivery system allowing the trajectory to be generated at a high rate, mitigating effects of the unknown winds. This paper provides derivation of the guidance and control algorithms and present analysis through simulation.

I. Introduction

MANEUVERABLE ram-air parafoils are widely used today. The list of users includes skydivers, smoke jumpers, and Special Forces to name a few. Furthermore, their extended range compared to round parachutes makes them very practical for payload delivery. For round canopy parachutes the current requirement for a drop zone (DZ) size for the High Velocity Container Delivery System from 2,500m altitude as defined in the Joint U.S. Army / U.S Air Force Field Manual 5-430-00-2[1] is as large as 780m by 1,610m or a 1,255,800m^2 (260 acres) footprint. During the latest humanitarian aid aerial delivery missions, such as the delivery of food, supplies and medications to war-torn areas like Bosnia, Sarajevo, Afghanistan, and Iraq 50% of payloads were never recovered. Such requirements for parafoils haven't been developed because high-glide ratio delivery systems cannot glide to a specific location by themselves, but rather require a guidance, navigation and control (GNC) unit to produce and track the corresponding steering commands.[2,3]

Recent introduction of the Global Positioning System (GPS) made the development of fully autonomous ram-air parafoils possible. Moreover, ram-air parafoils are considered a vital element of the unmanned air vehicles capability,[4-6] can be used in conjunction with a space station crew rescue,[7-10] and in some other applications.[11] Autonomous parafoil capability implies delivering the system to a desired landing point from an arbitrary (limited by winds, deployment condition and system performance) release point using an onboard computer, sensors and actuators. The navigation subsystem manages data acquisition, processes sensor data, and provides guidance and control subsystems with information about parafoil states. Using this information along with local wind profiles, the guidance subsystem plans the mission and generates a feasible trajectory to the desired landing point. Finally, it is the responsibility of the control system to track this trajectory using the information provided by the navigation subsystem and onboard actuators.

The need for development of the fully autonomous different-weight aerodynamic decelerator systems emerged just in the past decade. Natick Soldier Center, Natick, MA pursues and pushes the development of the new

* Assistant Professor, Department of Mechanical and Aerospace Engineering, slegers@mae.uah.edu, Member AIAA.

† Research Associate Professor, Department of Mechanical and Astronautical Engineering, Code MAE/Yk, oayakime@nps.edu, Associate Fellow AIAA.

generation joint precision aerodynamic delivery systems (JPADS) capable of achieving a breakthrough accuracy of less the 100m circular error probable (CEP).[12] The underlying concept to be employed on every system is to have a field-laptop-based JPADS Mission Planner (developed by Planning Systems, NOA/FSL and DL) that can predict the winds at different altitudes with unprecedented accuracy.[13-15] Wind prediction enables computation of the required release point from the airdrop cargo airplane. Improved Container Delivery System developed for 26' Ring Slot or G-12 unguided ballistic parachutes along with JPADS-Mission Planner allows reduction of the DZ to 109m by 219m or 23,937m^2 (5 acres), i.e. 52 times smaller then for the conventional systems that do not have the JPADS Mission Planner. The authors were lucky to participate in the program of the development of the Affordable Guided Aerodelivery Systems[16] that not only employed JPADS-Mission Planner, but also by relatively inexpensive means allowed conversion of regular ballistic (dumb) circular parachutes into a guided system.[17] The accuracy achieved with this system is even smaller than 5-acre-footprint and remains on the order of potentially more accurate parafoil-based systems.[18]

The ultimate goal for the perspective delivery system is to have payloads delivered from the large standoff distances with <100m CEP accuracy. So during the last decade, several GNC concepts for gliding parachute applications have been developed and published.[19-31] Specifically, the best systems were demonstrated during Precision Airdrop Technology Conference and Demonstration PATCAD-2001, PATCAD-2003, PATCAD-2005 and PATCAD-2007 at U.S. Army Yuma Proving Ground, Yuma, AZ, and Precision Airdrop Demonstration Capability PCAD-2006 and PCAD-2008 near Toulouse, France.[32-34]

Analyzing the results of dozens of airdrops it can be stated that the most accurate systems can only achieve 100m-150m accuracy (excluding SPADES by Dutch Space[25] that assures about 40m-60m accuracy). More detailed analysis reveals that GNC systems developed by Charles Stark Draper Laboratory,[20-24] Georgia Tech[29-31] and others implement simple proportional-integral-derivative (PID) controllers to track the reference heading, which is assigned based on a combination of some logics and heuristic rules. For the final stage of descent to the DZ some controllers use a moth mode, others attempted to utilize a precomputed landing trajectories data base.[24] Though some of the systems utilize JPADS Mission Planner they only use it to compute a release point, but they do not use its winds prediction during the following control.

This paper builds on the generic GNC algorithm developed earlier[27,28] and specifically concentrates on the terminal phase of guided descent, where the majority of errors contribute to the final touchdown accuracy. The paper is organized as follows. Section II overviews the overall control strategy consisting of six phases that follow each other upon loosing altitude during a descent. Section III features the Model Predictive Control (MPC) used to track the desired trajectory at each phase.[27,28] Section IV introduces a six degree-of-freedom model of a generic parafoil delivery system and characterizes the linearized model, developed for use with MPC. Section V provides details of the simple straightforward control algorithm during the final phase (turning base), while Section VI deals with the more sophisticated adaptive optimal control for this final phase. The paper ends with several computer simulations and conclusions.

II. Guidance Strategy

In the current design five parameters need to be defined by the user before deployment. The five parameters are: target location, away distance, cycle distance, turn diameter, and wind heading angle. These five parameters define five fixed tracking points, which are the Target, A, B, C, and D as shown in Fig.1. Using these five points, the ADS precision placement objectives are defined. As shown in Fig.1, trajectory planning for precision placement is divided into six phases. They are as follows:

- Phase 0: After canopy opening, guidance is delayed to allow oscillations to cease;
- Phase 1: The initial phase is used to reach the loitering area (bounded by points A, B, C, and D), where it is assumed that the system is released upwind of the loiter area;
- Phase 2: Loitering is commenced. The system estimates, winds, descent rate, and the altitude at which to turn towards the target. The loiter area is defined by four points A, B, C, and D. As stated above these four points are determined by the target location, wind direction, away distance, cycle distance, and turn diameter. During loiter, winds are estimated when traveling from A to B and from C to D (long parallel legs). Ideally, at least one complete loop around A, B, C, and D is completed. Winds, distance to the target, and vertical velocity are used to determine a switching altitude z_{start} to start the downwind leg towards the target (as explained in Section V). When the measured altitude reaches z_{start} Phase 2 is terminated and the system turns toward the target;
- Phase 3: Wind estimation is halted as the loiter area is exited;

- Phase 4: Wind estimate is reinitiated as the system travels toward the target. All estimated data is used to determine a distance D_{switch} past the target to make a final turn and approach. When the distance D_{switch} is reached Phase 5 is initiated;
- Phase 5: A 180-degree turn to the final approach glide slope;
- Phase 6: Final approach and landing into the wind.

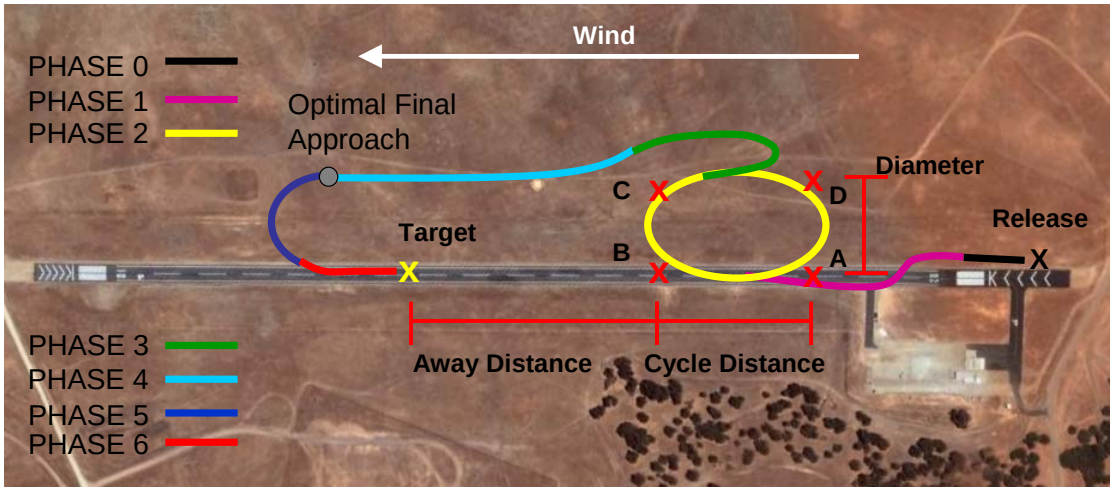

Fig.1 Guidance strategy.

The precision placement algorithm tracks a desired heading using a model predictive control (MPC) described in Sections III and IV. In each phase the current position and desired tracking points are used to determine a desired heading of the system. Prior to terminal guidance (phases 0 through 4) the desired heading is found simply by heading directly to the next tracking point. However, in the critical final phases the desired heading is found by rapidly calculating an optimal trajectory, detailed in Sections V and VI.

III. Model Predictive Control

Consider a simple Single-Input Single-Output (SISO) discrete system described in state space form as:

$$\begin{aligned} \mathbf{x}_{k+1} &= \mathbf{A}\mathbf{x}_k + \mathbf{B}u_k \\ y_k &= \mathbf{C}\mathbf{x}_k \end{aligned} \tag{1}$$

(Hereinafter bold font for lower-case symbols denotes vectors and bold font for upper-case symbols denotes matrices). Assume that the system matrices **A**, **B**, and **C** are known and that $\mathbf{x}_k$ is the state vector, u_k is the control input, and y_k is the output at time k. The model described above can be used to estimate the future state of the system. Assuming a desired trajectory w_k is known an estimated error signal $\hat{e}_k = w_k - \hat{y}_k$ is computed over a finite set of future time instants called the prediction horizon, H_p (hereinafter the symbol "^" is used to represent an estimated quantity). In model predictive control, the control computation problem is cast as a finite time discrete optimal control problem. To compute the control input at a given time instant, a quadratic cost function is minimized through the selection of the control history over the control horizon. The cost function can be written as:

$$J = \left(\mathbf{W} - \hat{\mathbf{Y}}\right)^T \mathbf{Q}\left(\mathbf{W} - \hat{\mathbf{Y}}\right) + \mathbf{U}^T\mathbf{R}\mathbf{U}\,, \tag{2}$$

where

$$\mathbf{W} = [w_{k+1}, w_{k+2}, \ldots, w_{k+H_p}]^T\,, \tag{3}$$

$$\hat{\mathbf{Y}} = \mathbf{K}_{CA}\mathbf{x}_k + \mathbf{K}_{CAB}\mathbf{U}\,, \tag{4}$$

$$\mathbf{U} = [u_k, u_{k+1}, \ldots, u_{k+H_p-1}]^T\,, \tag{5}$$

and both **R** and **Q** are symmetric positive semi-definite matrices of size H_p x H_p. Equation 1 is used to express the predicted output vector $\hat{\mathbf{Y}}$ in terms of the system matrices

$$\mathbf{K}_{CA} = \begin{bmatrix} \mathbf{CA} \\ \mathbf{CA}^2 \\ \vdots \\ \mathbf{CA}^{H_p} \end{bmatrix}, \tag{6}$$

$$\mathbf{K}_{CAB} = \begin{bmatrix} \mathbf{CB} & 0 & 0 & 0 & 0 \\ \mathbf{CAB} & \mathbf{CB} & 0 & 0 & 0 \\ \mathbf{CA}^2\mathbf{B} & \mathbf{CAB} & \mathbf{CB} & 0 & 0 \\ \vdots & \vdots & \vdots & \ddots & 0 \\ \mathbf{CA}^{H_p-1}\mathbf{B} & \cdots & \mathbf{CA}^2\mathbf{B} & \mathbf{CAB} & \mathbf{CB} \end{bmatrix}. \tag{7}$$

The first term in Eq.(2) penalizes tracking error, while the second term penalizes control action. Equations (2), (6), and (7) can be combined resulting in the cost function

$$J = \left(\mathbf{W} - \mathbf{K}_{CA}\mathbf{x}_k - \mathbf{K}_{CAB}\mathbf{U}\right)^T \mathbf{Q}\left(\mathbf{W} - \mathbf{K}_{CA}\mathbf{x}_k - \mathbf{K}_{CAB}\mathbf{U}\right) + \mathbf{U}^T\mathbf{R}\mathbf{U} \tag{8}$$

that is now expressed in terms of the system state $\mathbf{x}_k$, desired trajectory **W**, control vector **U** and system matrices **A**, **B**, **C**, **Q**, and **R**.

The control **U**, which minimizes Eq.(8), can be found analytically as

$$\mathbf{U} = \mathbf{K}\left(\mathbf{W} - \mathbf{K}_{CA}\mathbf{x}_k\right), \tag{9}$$

where

$$\mathbf{K} = \left(\mathbf{K}_{CAB}^T\mathbf{Q}\mathbf{K}_{CAB} + \mathbf{R}\right)^{-1}\mathbf{K}_{CAB}^T\mathbf{Q}. \tag{10}$$

Equation 10 contains the optimal control inputs over the entire control horizon, however at time *k* only the first element u_k is needed. The first element u_k can be extracted from Eq.(9) by defining $\mathbf{K}_1$ as the first row of **K**. The optimal control over the next time sample becomes

$$u_k = \mathbf{K}_1\left(\mathbf{W} - \mathbf{K}_{CA}\mathbf{x}_k\right), \tag{11}$$

where calculation of the first element of the optimal control sequence requires the desired trajectory **W** over the prediction horizon and the current state $\mathbf{x}_k$.

IV. Parafoil Modeling

The full combined flexible system of the parafoil canopy and the payload can be represented as a 9 or 8 degree-of-freedom (DoF) model depending on the specific harness connecting these two pieces together. Alternatively it can also be modeled as a solid structure requiring only six-DoF, which include three inertial position components of the system mass center as well as the three Euler orientation angles of the parafoil-payload system. This section first introduces a six-DoF model of a generic parafoil system that will be used for simulation and GNC algorithm development, and then addresses a simplified model used to compute the MPC gains appearing in Eq.(11).

A. Six DoF Model

Figure 2 shows a schematic of a parafoil and payload system. With the exception of movable parafoil brakes, the parafoil canopy is considered to be a fixed shape once it has completely inflated. A body frame $\{B\}$ is fixed at the system mass center with the unit vectors $\mathbf{i}_B$ and $\mathbf{k}_B$ orientated forward and down. Orientation of the parafoil canopy with respect to the body frame is defined as the incidence angle Γ.

Orientation of the body frame $\{B\}$ is obtained by a sequence of three body-fixed rotations. Starting from the inertial frame $\{I\}$, the system is successively rotated through Euler yaw ψ, pitch θ, and roll φ. The resulting transformation from the inertial to body frame is

$$\mathbf{T}_{IB} = \begin{bmatrix} c_\theta c_\psi & c_\theta s_\psi & -s_\theta \\ s_\phi s_\theta c_\psi - c_\phi s_\psi & s_\phi s_\theta s_\psi + c_\phi c_\psi & s_\phi c_\theta \\ c_\phi s_\theta c_\psi + s_\phi s_\psi & c_\phi s_\theta s_\psi - s_\phi c_\psi & c_\phi c_\theta \end{bmatrix}, \tag{12}$$

where the common shorthand notation for trigonometric functions is employed, so that for any angle α $\sin(\alpha) \equiv s_\alpha$ and $\cos(\alpha) \equiv c_\alpha$. Translation kinematics of the system become

$$\begin{bmatrix} \dot{x} \\ \dot{y} \\ \dot{z} \end{bmatrix} = \mathbf{T}_{IB}^T \begin{bmatrix} u \\ v \\ w \end{bmatrix}, \tag{13}$$

where *x, y*, and *z* are the inertial positions and *u, v*, and *w* are body frame velocities. Defining the angular velocity of the parafoil payload system as:

$$\boldsymbol{\omega}_{B/I} = p\mathbf{i}_B + q\mathbf{j}_B + r\mathbf{k}_B \tag{14}$$

results in the following rotational kinematics equations:

$$\begin{bmatrix} \dot{\phi} \\ \dot{\theta} \\ \dot{\psi} \end{bmatrix} = \begin{bmatrix} 1 & s_\phi t_\theta & c_\phi t_\theta \\ 0 & c_\phi & -s_\phi \\ 0 & s_\phi c_\theta^{-1} & c_\phi c_\theta^{-1} \end{bmatrix} \begin{bmatrix} p \\ q \\ r \end{bmatrix} \tag{15}$$

($t_\alpha \equiv \tan(\alpha)$).

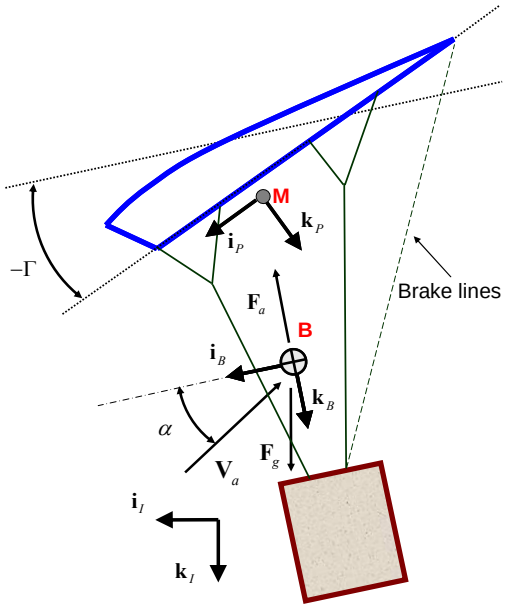

Fig.2 A generic 6-DoF parafoil-payload system.

Forces and moments acting on the parafoil and payload have contributions from: weight, aerodynamic loads, and apparent mass of the canopy. Weight contribution of the system is expressed in the body frame,

$$\mathbf{F}_g = \begin{bmatrix} -s_\theta \\ s_\phi c_\theta \\ c_\phi c_\theta \end{bmatrix} mg, \tag{16}$$

with *m* being the system mass and *g* the acceleration from gravity. Aerodynamic forces and moments have contributions from both the canopy and payload. Both canopy and payload contributions are combined into a single aerodynamic model using standard aerodynamic derivatives. The aerodynamic force is modeled as:

$$\mathbf{F}_a = \mathbf{T}_{AB} \frac{\rho V_a^2 S_p}{2} \begin{bmatrix} C_{D0} + C_{D\alpha 2}\alpha^2 \\ C_{Y\beta}\beta \\ C_{L0} + C_{L\alpha}\alpha \end{bmatrix}, \tag{17}$$

where; α and β are the angle of attack and sideslip of the body frame, V_a is the true airspeed, S_p is the parafoil canopy area, and $\mathbf{T}_{AB}$ is the transformation from the aerodynamic to body frame by the angle of attack α. Similarly, the aerodynamic moment is written as:

$$\mathbf{M}_a = \frac{\rho V_a^2 S_p}{2}\begin{bmatrix} b(C_{l\beta} + \frac{b}{2V_a}C_{lp}) + \frac{b}{2V_a}C_{lr}r + \bar{d}^{-1}C_{l\delta a}\delta_a) \\ \bar{c}(C_{m0} + C_{m\alpha}\alpha + \frac{\bar{c}}{2V_a}C_{mq}q) \\ b(C_{n\beta} + \frac{b}{2V_a}C_{np}p + \frac{b}{2V_a}C_{nr}r + \bar{d}^{-1}C_{n\delta a}\delta_a) \end{bmatrix} \tag{18}$$

where, b and $\bar{c}$ are the canopy span and chord, δ_a is the asymmetric brake deflection, and $\bar{d}$ is the maximum brake deflection. Parafoil canopies with small mass to volume ratios can experience large forces and moments from accelerating fluid called "apparent mass." They appear as additional mass and inertia values in the final equations of motion. Parafoil canopies with small arch-to-span ratios and negligible camber can be approximated to useful accuracy by an ellipsoid having three planes of symmetry; however, the planes of symmetry in the canopy frame may not be aligned with the body frame, as shown in Fig.2. Apparent mass forces and moments for an approximately ellipsoidal canopy can be conveniently defined using the translation and angular velocities expressed in the canopy frame $\{P\}$. Defining $\mathbf{T}_{BP}$ as the single axis transformation from the body to canopy reference frame by the incidence angle Γ, $\mathbf{r}_{BM} = [x_{BM}, y_{BM}, z_{BM}]^T$ as the vector from the system mass center to the apparent mass center, and $\mathbf{W}$ as the wind vector, the velocity of the canopy at the apparent mass center can be expressed in the canopy frame as:

$$\begin{bmatrix} \tilde{u} \\ \tilde{v} \\ \tilde{w} \end{bmatrix} = \mathbf{T}_{BP}\left(\begin{bmatrix} u \\ v \\ w \end{bmatrix} + \mathbf{S}^B_{\boldsymbol{\omega}}\begin{bmatrix} x_{BM} \\ y_{BM} \\ z_{BM} \end{bmatrix} - \mathbf{T}_{IB}\mathbf{W}\right), \tag{19}$$

where the second term represents the vector cross product using the skew-symmetric matrix $\mathbf{S}^B_{\omega}$, constructed as follows:

$$\mathbf{S}^A_{\boldsymbol{\xi}} = \begin{bmatrix} 0 & -\xi_z & \xi_y \\ \xi_z & 0 & -\xi_x \\ -\xi_y & \xi_x & 0 \end{bmatrix} \tag{20}$$

(here ξ_x, ξ_y and ξ_z are the components of vector $\boldsymbol{\xi}$ expressed in a coordinate frame $\{A\}$).

Similarly, the angular velocity expressed in the canopy frame $\{P\}$ becomes

$$\begin{bmatrix} \tilde{p} \\ \tilde{q} \\ \tilde{r} \end{bmatrix} = \mathbf{T}_{BP}\begin{bmatrix} p \\ q \\ r \end{bmatrix}. \tag{21}$$

Forces and moments from apparent mass and inertia are then found by relating the fluid's kinetic energy to resultant forces and moments.[35] Apparent mass and inertia contributions expressed in the body frame can be written as:

$$\mathbf{F}_{a.m.} = -\mathbf{T}^T_{BP}\left(\mathbf{I}_{a.m.}\begin{bmatrix} \dot{\tilde{u}} \\ \dot{\tilde{v}} \\ \dot{\tilde{w}} \end{bmatrix} + \mathbf{S}^P_{\boldsymbol{\omega}}\mathbf{I}_{a.m.}\begin{bmatrix} \tilde{u} \\ \tilde{v} \\ \tilde{w} \end{bmatrix}\right), \tag{22}$$

$$\mathbf{M}_{a.i.} = -\mathbf{T}^T_{BP}\left(\mathbf{I}_{a.i.}\begin{bmatrix} \dot{\tilde{p}} \\ \dot{\tilde{q}} \\ \dot{\tilde{r}} \end{bmatrix} + \mathbf{S}^P_{\boldsymbol{\omega}}\mathbf{I}_{a.i.}\begin{bmatrix} \tilde{p} \\ \tilde{q} \\ \tilde{r} \end{bmatrix}\right), \tag{23}$$

where

$$\mathbf{I}_{a.m.} = \begin{bmatrix} A & 0 & 0 \\ 0 & B & 0 \\ 0 & 0 & C \end{bmatrix} \text{ and } \mathbf{I}_{a.i.} = \begin{bmatrix} P & 0 & 0 \\ 0 & Q & 0 \\ 0 & 0 & R \end{bmatrix}. \tag{24}$$

(Apparent mass and inertia values A, B, C, P, Q, and R appearing in Eq.(24) can be calculated for known simple shapes or can be approximated as discussed in Ref.35.)

Dynamic equations are formed by summing forces and moments about the system mass center, both in the body reference frame, and equating to the time derivative of linear and angular momentum. Final dynamic equations of motion are expressed compactly in matrix form below, where for the quantities in Eq.(24) the common convention is used for tensors of second rank such that $\mathbf{I}'_{\xi} = \mathbf{T}_{BP}^{T}\mathbf{I}_{\xi}\mathbf{T}_{BP}$:

$$\begin{bmatrix} m\mathbf{I}_{3\times 3}+\mathbf{I}'_{a.m.} & \cdots & -\mathbf{I}'_{a.m.}\mathbf{S}^{B}_{r_{BM}} \\ \cdots & \cdots & \cdots \\ \mathbf{S}^{B}_{\mathbf{r}_{BM}}\mathbf{I}'_{a.m.} & & \mathbf{I}+\mathbf{I}'_{a.i.}-\mathbf{S}^{B}_{\mathbf{r}_{BM}}\mathbf{I}'_{a.m.}\mathbf{S}^{B}_{\mathbf{r}_{BM}} \end{bmatrix} \begin{bmatrix} \dot{u} \\ \dot{v} \\ \dot{w} \\ \cdots \\ \dot{p} \\ \dot{q} \\ \dot{r} \end{bmatrix} = \begin{bmatrix} \mathbf{F} \\ \cdots \\ \mathbf{M} \end{bmatrix}, \tag{25}$$

where $\mathbf{I}_{3\times 3}$ is the identity matrix, $\mathbf{I} = \begin{bmatrix} I_{xx} & 0 & I_{xz} \\ 0 & I_{yy} & 0 \\ I_{xz} & 0 & I_{zz} \end{bmatrix}$,

$$\mathbf{F} = \mathbf{F}_a + \mathbf{F}_g - m\mathbf{S}^{B}_{\boldsymbol{\omega}} \begin{bmatrix} u \\ v \\ w \end{bmatrix} - \mathbf{T}^{T}_{BP}\mathbf{S}^{P}_{\boldsymbol{\omega}}\mathbf{I}_{a.m.} \begin{bmatrix} \tilde{u} \\ \tilde{v} \\ \tilde{w} \end{bmatrix} - \mathbf{I}'_{a.m.}\mathbf{S}^{B}_{\boldsymbol{\omega}}\mathbf{T}_{IB}\mathbf{W}, \tag{26}$$

$$\mathbf{M} = \mathbf{M}_a - \mathbf{S}^{B}_{\boldsymbol{\omega}}\mathbf{I} \begin{bmatrix} p \\ q \\ r \end{bmatrix} - \mathbf{S}^{B}_{\mathbf{r}_{BM}}\mathbf{T}^{T}_{BP}\mathbf{S}^{P}_{\boldsymbol{\omega}}\mathbf{I}_{a.m.} \begin{bmatrix} \tilde{u} \\ \tilde{v} \\ \tilde{w} \end{bmatrix} - \mathbf{T}^{T}_{BP}\mathbf{S}^{P}_{\boldsymbol{\omega}}\mathbf{I}_{a.i.} \begin{bmatrix} \tilde{p} \\ \tilde{q} \\ \tilde{r} \end{bmatrix} + \mathbf{S}^{B}_{\mathbf{r}_{BM}}\mathbf{I}'_{a.m.}\mathbf{S}^{B}_{\boldsymbol{\omega}}\mathbf{T}_{IB}\mathbf{W}. \tag{27}$$

B. Linearized Model

The guidance strategy outlined in Section II requires a simple SISO controller with yaw as an output and the brake deflection δ_a as the control. A simple 2-DoF model of the roll and yaw dynamics is used since for parafoils pitch and speed are not typically controllable. The state vector **x** for the 2-DoF rotational model contains roll, yaw, roll rate, and yaw rate:

$$\mathbf{x} = [\phi, \psi, p, r]^{T}. \tag{28}$$

Equations (15) and (25) describe the nonlinear rotational kinematics and dynamics. However, for MPC (1) a linear discrete model is required. Assuming that the aerodynamic velocity V_a is constant, Eqs.(15) and (25) can be numerically linearized about the steady state

$$\mathbf{s}_0 = \begin{bmatrix} \phi_0 \\ \theta_0 \\ p_0 \\ q_0 \\ r_0 \\ \delta_{a0} \end{bmatrix} = \begin{bmatrix} 0 \\ \theta_0 \\ 0 \\ 0 \\ 0 \\ 0 \end{bmatrix}. \tag{29}$$

With the convention $\mathbf{s}^{*} = \mathbf{s} - \mathbf{s}_0$ t the resulting linear discrete model for the parafoil with parameters listed in the Appendix and sampling period of 0.5s is:

$$\begin{bmatrix} \phi^{*} \\ \psi^{*} \\ \dot{p}^{*} \\ \dot{r}^{*} \end{bmatrix}_{k+1} = \begin{bmatrix} 0.962 & 0 & 0.153 & 0.012 \\ 0.0078 & 1 & -0.011 & 0.043 \\ -0.103 & 0 & 0.033 & 0.004 \\ 0.0191 & 0 & -0.0023 & -0.003 \end{bmatrix} \begin{bmatrix} \phi^{*} \\ \psi^{*} \\ p^{*} \\ r^{*} \end{bmatrix}_{k} + \begin{bmatrix} -0.006 \\ 0.0501 \\ -0.0131 \\ 0.1098 \end{bmatrix} \delta_{a;k}. \tag{30}$$

Matrices given by Eq.(30), along with the output matrix **C** = [0 1 0 0] define the optimal brake deflection δ_a according to the MPC algorithm in Eq.(11).

V. Terminal Guidance

The last three phases introduced in Section II (Phases 4-6) are the most critical stages of parafoil guidance. The system must be dropped up wind of the target to ensure it can be reached, however, it is desired to impact the target traveling into the wind to reduce ground speed. In addition it is beneficial to arrive near the target with excess altitude in order to make final guidance decisions. Finally, there is a very strict time limitation. The ADS can be slightly late or earlier departing/arriving to all other phases, but this last Phase 6 ends sharply at landing. All this means that special precautions have to be made in building a control algorithm for the terminal phase.

First, assume that there is no cross wind component, i.e. that the ground winds uploaded to the system before deployment have not changed. An ideal terminal guidance trajectory can be defined as outlined in Fig.3, where the following notations are used (Fig.3 represents the left approach pattern, but everything will be the same for the right pattern as well.):

x, y, z – a standard right-handed North-East-Down coordinate frame with the origin at the target;

t_{start} – time corresponding to the beginning of the downwind leg (Phase 4);

t_0 – time corresponding to the beginning of the final 180°-turn (Phase 5);

t_1 – time corresponding to intercepting the final approach (Phase 6);

t_{exit} – time when guidance switches from Phase 5 to Phase 6;

t_2 – time of touchdown;

L – distance away from the target line;

D_{switch} – optimal distance to pass the target (initiating a final turn at t_0 should achieve the desired impact location);

$T_{turn} = t_1 - t_0$ – final turn time;

$T_{app} = t_2 - t_1$ – final approach time, determining t_0 and D_{switch} (a large value allows correction for terminal errors and reduces errors from changing winds, while a small value reduces errors during final approach);

R – final turn radius;

W – wind (positive when coming from the x_I direction and negative as shown in Fig.2);

$\psi(t)$ – final turn function for parafoil to track during the final turn;

$\tilde{D} = WT_{turn}$ – distance defined by imperfection (asymmetry) of the final turn because of the wind.

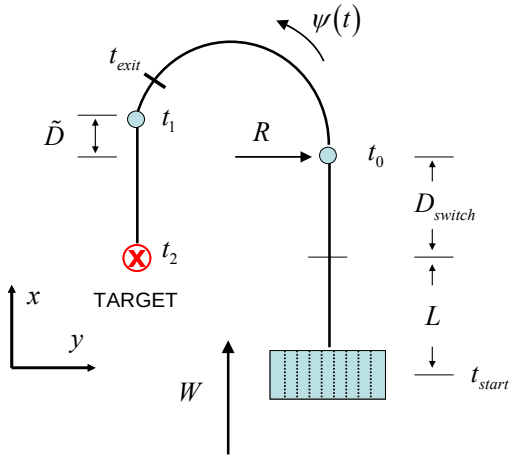

Fig.3 Terminal guidance maneuver.

The terminal guidance problem can be summarized as follows. For a parafoil in the presence of wind W, at altitude z, and a distance L from the target, find the distance D_{switch} to the final turn initiation point (TIP), required to travel past the target for an ideal impact at t_2 (of course, D_{switch} is a function of the desired T_{app}^{des}.)

In general, the dynamic model of a parafoil is complex and nonlinear, so that the problem can only be solved numerically. However, in what follows we will make some assumptions, allowing an analytical solution to be used as a reference trajectory in the control algorithm. These assumptions are: a) the turn rate is slow, so that the roll and sideslip angles can be ignored, and b) the descent rate V_v^* and air speed V_h^* are viewed as nearly constant (defined by the canopy, lines, etc. and treated as the known values). In this case it immediately follows that

$$t_2 = t_{start} - \frac{z_{start}}{V_v^*}. \tag{31}$$

The problem reduces to handling a simple kinematic model represented by three components of the ground velocity as:

$$\begin{bmatrix}\dot{x}\\ \dot{y}\\ \dot{z}\end{bmatrix}=\begin{bmatrix}-W+V_h^*\cos\psi\\ V_h^*\sin\psi\\ V_v^*\end{bmatrix}. \tag{32}$$

Now, the reference turn function $\psi(t)$ can be chosen as any function that satisfies the boundary conditions $\psi(t_0)=0$ and $\psi(t_1)=-\pi$ (for the left pattern as shown on Fig.3). For instance, for a linear turn (constant turn rate) the solution to the required turn rate and the final turn time T_{turn} are provided by:

$$\dot{\psi}=-\frac{V_h^*}{R} \quad \text{and} \quad T_{turn}=\frac{\pi R}{V_h^*}. \tag{33}$$

Hence, the most straightforward algorithm to control the descending system at the terminal phase is to control its turn rate for example as follows:

$$\dot{\psi}^c=\mp\frac{V_h^*}{R} \tag{34}$$

(the plus-minus signs correspond to the left and right turn, respectively). After the final turn the system travels directly to the desired target. Assuming that the wind W is constant all way down and a constant turn rate (33), integration of inertial velocities along axes *x* and *y* from t_{start} to t_2 (Phases 4-6) yields two simple equalities:

$$D_{switch}-\int_{t_0}^{t_1}\dot{x}dt-\int_{t_1}^{t_2}\dot{x}dt=D_{switch}-WT_{turn}-(V_h^*+W)T_{app}=0, \tag{35}$$

$$z+V_v^*\left(\frac{L+D_{switch}}{V_h^*-W}\right)+V_v^*t_{turn}+V_v^*t_{app}=0. \tag{36}$$

Resolving them with respect to D_{switch} and a T_{app} results in

$$D_{switch}=WT_{turn}+\left(\frac{V_h^{*2}-W^2}{2V_h^*}\right)\left(\frac{-z}{V_v^*}-T_{turn}-\frac{L+WT_{turn}}{V_h^*-W}\right), \tag{37}$$

$$T_{app}=\left(\frac{V_h^*-W}{2V_h^*}\right)\left(\frac{-z}{V_v^*}-T_{turn}\right)-\frac{L+WT_{turn}}{2V_h^*}. \tag{38}$$

From Eqs.(37) and (38) it can be seen that the higher the altitude z, the larger D_{switch} and T_{app} become. As the parafoil loiters upwind of the target, z_{start} the altitude at which to turn towards the target can be found by using a desired final approach time T_{app}^{des}. The switching altitude to achieve T_{app}^{des} is then given by solving Eq.(38) for z leading to the following expression:

$$z_{start}=-V_v^*\left(T_{turn}+\frac{L+WT_{turn}}{V_h^*-W}+\frac{2V_h^*}{V_h^*-W}T_{app}^{des}\right)=V_v^*\frac{L+V_h^*(T_{turn}+2T_{app}^{des})}{W-V_h^*}. \tag{39}$$

Once the system is traveling towards the target the goal is to bring the system from its initial state at the top of the downwind led to the point defined by $x_T=D_{switch}$ and $y_T=\mp 2R$ (for the left and right turn, respectively). The distance $\hat{D}_{switch}$ is estimated during the downwind leg constantly using the analogue of Eq.(37):

$$\hat{D}_{switch}=\hat{W}T_{turn}+\left(\frac{\hat{V}_h^{*2}-\hat{W}^2}{2\hat{V}_h^*}\right)\left(\frac{-\hat{z}}{\hat{V}_v^*}-T_{turn}-\frac{\hat{x}+\hat{W}T_{turn}}{\hat{V}_h^*-\hat{W}}\right)=-\frac{\hat{z}(\hat{V}_h^{*2}-\hat{W}^2)+\hat{V}_h^*\hat{V}_v^*T_{turn}(\hat{V}_h^*-\hat{W})+\hat{x}\hat{V}_v^*(\hat{V}_h^*+\hat{W})}{2\hat{V}_h^*\hat{V}_v^*}, \tag{40}$$

where $\hat{V}_h^*$, $\hat{V}_v^*$ and $\hat{W}$ are the estimates of the corresponding parameters at current position ($\hat{x}$, $\hat{z}$). Note, Eq.(40) produces the value of $\hat{D}_{switch}$ in the assumption that V_h^*, V_v^* and W remain constant from the current altitude all way down.

Figure 4 demonstrates simulation results for the ideal case when all parameters (horizontal airspeed, descent rate, wind) are assumed to be estimated with no errors, there are no disturbances, and the commanded yaw rate is tracked precisely. Specifically, for horizontal airspeed of 22.4ft/s, descent rate of 10ft/s, wind of -10ft/s, turn radius of 125ft,

and the desired final approach time T_{app}^{des} of 7.5s, the maneuver starts at the altitude of 561.36ft (L=750ft). The distance D_{switch} is estimated to be -82.3ft, it takes 17.5s to make a full turn, and the system touches down precisely on target in 45.65s.

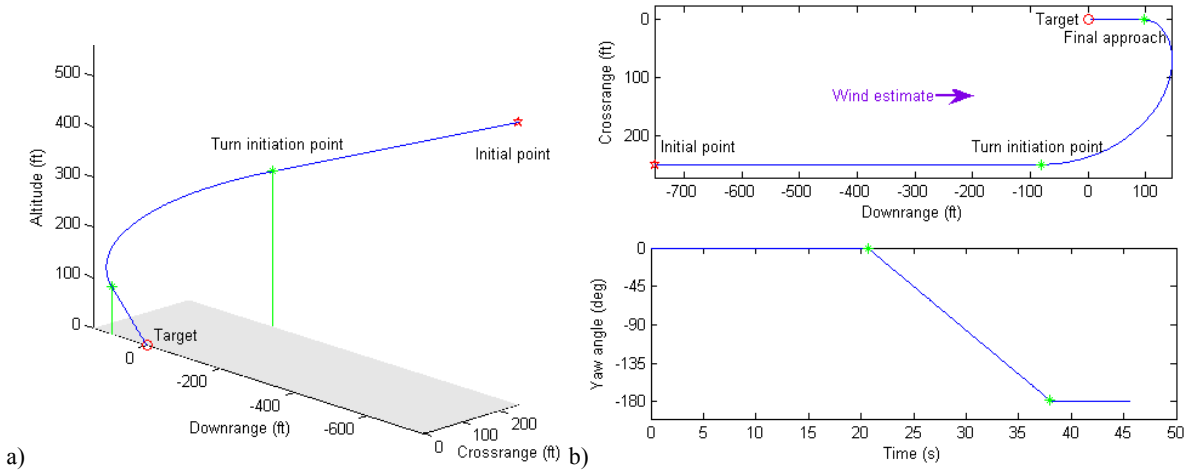

Fig.4 Simulated guidance in ideal conditions: 3D trajectory (a), horizontal projection and the time history of the yaw angle (b).

In practice, sensor errors, variable winds (magnitude and direction), and imperfect control will certainly disturb the ideal touchdown depicted above. For example, Table 1 provides measurement errors typical for the GNC unit used. Winds can change (and are changing) all the time. Let us illustrate how inaccuracies in measuring ADS position errors arriving at the TIP and variable winds may affect the touchdown accuracy.

Table 1. Errors in measuring the ADS states.

Parameter	Bias	Standard deviation
Altitude z	10 ft	1 ft
Descent rate $\dot{z}$	0 ft/s	2 ft/s
Roll angle ϕ	1.5 °	1.5 °
Yaw angle ψ	3 °	1.5 °
Roll rate p	1 °/s	1.5 °/s
Yaw rate r	1 °/s	1.5 °/s

Figure 5 shows Monte Carlo simulations where two cases were considered. First, it was assumed that the downwind leg ends up with some error in the ADS horizontal position and heading. The standard deviation of horizontal position error in each coordinate was assumed to be 20ft and the standard deviation in heading 10 °. As seen from Fig.5a these errors result in spreading the arrival to the final approach point. The situation is even worse when unaccounted winds are acting on the ADS during the final turn.

For simulations shown in Fig.5b, the standard deviation for wind disturbances applied at each integration step of 0.05s was only 3ft/s (with a zero mean value) in both x and y direction, but as shown it led to a drastic degradation of the overall performance. Obviously, if we add a constant (unmeasured wind) that acts on the system all way down in any direction it will simply blow the ADS off the desired trajectory. This is the worst case scenario. Now the question is how to mitigate the effect of changing winds?

The control algorithm only provides indirect estimates of the wind based on the difference between the parafoil's measured ground speed and its steady state speed components, V_v^* and V_h^*. Again, these estimates are only valid for the current altitude and provide no prediction of future winds at lower altitudes. Therefore, rather than trying to better estimate current winds, the authors proceeded with the development of a robust algorithm accounting for constantly varying winds during the final turn and compensate for them by changing the yaw rate command. The next section addresses this algorithm based on the inverse dynamics in the virtual domain in more detail.

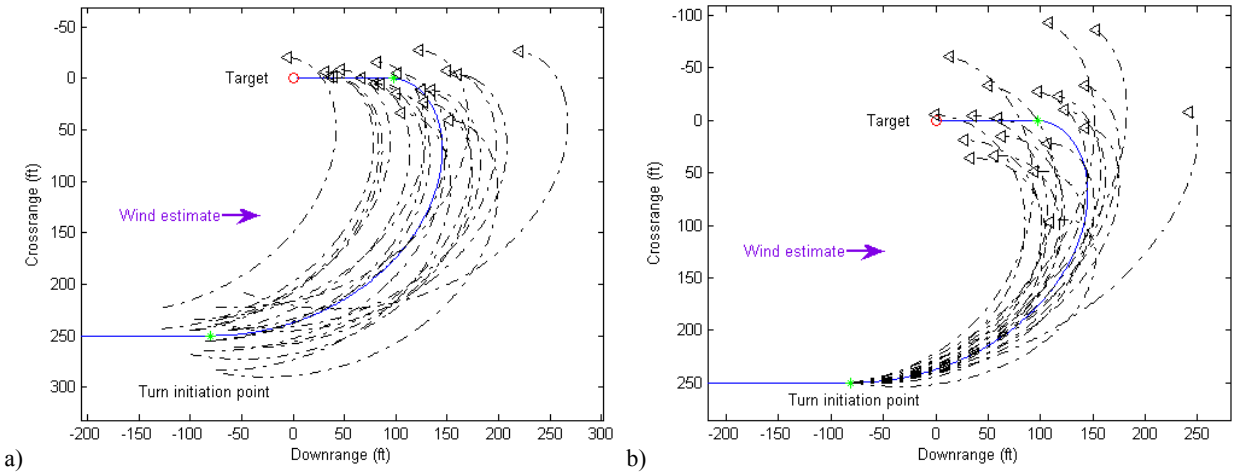

Fig.5 Final turn trajectories with not precise initial conditions (a) and unaccounted winds (b).

VI. Optimal Terminal Guidance

To overcome the difficulties of fighting unaccounted winds the following two-point boundary-value problem (TPBVP) was formulated. Staring at some initial point at $t = 0$ with the state vector defined as $\mathbf{x}_0 = \left[x_0, y_0, \psi_0\right]^T$ we need to bring our ADS influenced by the last known constant wind $\mathbf{w} = \left[W, 0, 0\right]^T$ to another point, $\mathbf{x}_f = \left[\left(V_h^* + W\right)T_{app}^{des}, 0, -\pi\right]^T$ (for consistency with the previous section we will consider a left pattern turn) at $t = t_f$. Hence, we need to find the trajectory that satisfies these boundary conditions along with a constraint imposed on control (yaw rate), $\left|\dot{\psi}\right| \le \dot{\psi}_{\max}$, while finishing the maneuver in exactly T_{turn} seconds (if needed, the performance index may also include additional terms related to the compactness of the maneuver and/or control expenditure). The found optimal control $\dot{\psi}_{opt}(t)$ is then tracked by the ADS GNC unit using the MPC algorithm in Sections III and IV. Unaccounted winds $\mathbf{w}^{dist} = \left[w_x, w_y, 0\right]^T$ (the vertical component will be accounted for indirectly via estimating the current $\hat{V}_v$) will not allow exact tracking of the calculated optimal trajectory. Computation of the optimal trajectory will be updated during the final turn, each time starting from the current (off the original trajectory) initial conditions, requiring the ADS to be at $\mathbf{x}_f = \left[\left(V_h^* + W\right)T_{app}^{des}, 0, -\pi\right]^T$ in T_{turn} seconds from the beginning of the turn. The remaining time until arrival at the final approach is computed as

$$t_f = -\frac{\hat{z}}{\hat{V}_v} - T_{app}^{final}, \tag{41}$$

where T_{app}^{final} is the final calculated approach time from Eq.(38) before entering the final turn.

Development of the optimal trajectory algorithm begins by recalling from Eq.(32) the horizontal trajectory knimematics:

$$\begin{bmatrix} \dot{x} \\ \dot{y} \end{bmatrix} = \begin{bmatrix} -W + V_h^* \cos\psi \\ V_h^* \sin\psi \end{bmatrix}. \tag{42}$$

Recognizing that if the final turn horizontal trajectory is given by Eq.(42) the yaw angle along this trajectory is related to the change of inertial coordinates as follows:

$$\psi = \tan^{-1}\frac{\dot{y}}{\dot{x} + W}. \tag{43}$$

Differentiating (43) provides the yaw rate control required to follow the reference final turn trajectory in presence of constant wind W:

$$\dot{\psi} = \frac{\ddot{y}(\dot{x}+W) - \ddot{x}\dot{y}}{(\dot{x}+W)^2 + \dot{y}^2}\,. \tag{44}$$

The inertial (ground) speed along the trajectory will also depend on the current yaw angle:

$$\left|V_G\right| = \sqrt{\dot{x}^2 + \dot{y}^2} = \sqrt{V_h^{*2} + W^2 - 2V_h^* W\cos\psi}\,. \tag{45}$$

Now, following the general idea of direct methods of calculus of variations (e.g., see Ref.36) we will assume the solution of the TPBVP to be represented analytically as functions of some scaled abstract argument $\overline{\tau} = \tau / \tau_f \in [0;1]$:

$$\begin{aligned} x(\overline{\tau}) &= P_1(\overline{\tau}) = a_0^1 + a_1^1\overline{\tau} + a_2^1\overline{\tau}^2 + a_3^1\overline{\tau}^3 + b_1^1\sin(\pi\overline{\tau}) + b_2^1\sin(2\pi\overline{\tau}),\\ y(\overline{\tau}) &= P_2(\overline{\tau}) = a_0^2 + a_1^2\overline{\tau} + a_2^2\overline{\tau}^2 + a_3^2\overline{\tau}^3 + b_1^2\sin(\pi\overline{\tau}) + b_2^2\sin(2\pi\overline{\tau}). \end{aligned} \tag{46}$$

The coefficients a_i^η and b_i^η ($\eta = 1,2$) in these formulas are defined by the boundary conditions up to the second-order derivative at $\tau = 0$ and $\tau = \tau_f$ ($\overline{\tau} = 1$). According to the problem formulation and Eq.(42) these boundary conditions are as follows:

$$\begin{bmatrix} x \\ y \end{bmatrix}_{\tau=0} = \begin{bmatrix} x_0 \\ y_0 \end{bmatrix}, \begin{bmatrix} \dot{x} \\ \dot{y} \end{bmatrix}_{\tau=0} = \begin{bmatrix} -W + V_h^*\cos\psi_0 \\ V_h^*\sin\psi_0 \end{bmatrix}, \begin{bmatrix} \ddot{x} \\ \ddot{y} \end{bmatrix}_{\tau=0} = \begin{bmatrix} -\dot{\psi}_0 V_h^*\sin\psi_0 \\ \dot{\psi}_0 V_h^*\cos\psi_0 \end{bmatrix}, \tag{47}$$

$$\begin{bmatrix} x \\ y \end{bmatrix}_{\tau=\tau_f} = \begin{bmatrix} \left(V_h^* + W\right)T_{app}^{des} \\ 0 \end{bmatrix}, \begin{bmatrix} \dot{x} \\ \dot{y} \end{bmatrix}_{\tau=\tau_f} = \begin{bmatrix} -W - V_h^* \\ 0 \end{bmatrix}, \begin{bmatrix} \ddot{x} \\ \ddot{y} \end{bmatrix}_{\tau=\tau_f} = \begin{bmatrix} 0 \\ 0 \end{bmatrix}. \tag{48}$$

While the final conditions (48) will be constant (the second derivatives are zeroed for a smooth arrival), the initial conditions will reflect the current state of the system at each cycle of optimization. Let us now differentiate Eqs.(46) two times with respect to τ to get:

$$\begin{aligned} \tau_f P_\eta'(\overline{\tau}) &= a_1^\eta + 2a_2^\eta\overline{\tau} + 3a_3^\eta\overline{\tau}^2 + \pi b_1^\eta\cos(\pi\overline{\tau}) + 2\pi b_2^\eta\cos(2\pi\overline{\tau}),\\ \tau_f^2 P_\eta''(\overline{\tau}) &= 2a_2^\eta + 6a_3^\eta\overline{\tau} - \pi^2 b_1^\eta\sin(\pi\overline{\tau}) - (2\pi)^2 b_2^\eta\sin(2\pi\overline{\tau}). \end{aligned} \tag{49}$$

Equating these derivatives at the terminal points to the known boundary conditions (47)-(48) yields a system of linear algebraic equations to solve for coefficients a_i^η and b_i^η ($\eta = 1,2$). For instance, for the *x*-coordinate we'll get

$$\begin{bmatrix} 1 & 0 & 0 & 0 & 0 & 0 \\ 1 & 1 & 1 & 1 & 0 & 0 \\ 0 & 1 & 0 & 0 & \pi & 2\pi \\ 0 & 1 & 2 & 3 & -\pi & 2\pi \\ 0 & 0 & 2 & 0 & 0 & 0 \\ 0 & 0 & 2 & 6 & 0 & 0 \end{bmatrix} \begin{bmatrix} a_0^1 \\ a_1^1 \\ a_2^1 \\ a_3^1 \\ b_1^1 \\ b_2^1 \end{bmatrix} = \begin{bmatrix} x_0 \\ x_f \\ x_0'\tau_f \\ x_f'\tau_f \\ x_0''\tau_f^2 \\ x_f''\tau_f^2 \end{bmatrix} \tag{50}$$

Being resolved this system yields

$$\begin{aligned} &a_0^1 = x_0, \quad a_1^1 = -(x_0 - x_f) + \frac{(2x_0'' + x_f'')\tau_f^2}{6}, \quad a_2^1 = \frac{x_0''\tau_f^2}{2}, \quad a_3^1 = -\frac{(x_0'' - x_f'')\tau_f^2}{6};\\ &b_1^1 = \frac{2(x_0' - x_f')\tau_f + (x_0'' + x_f'')\tau_f^2}{4\pi}, \quad b_2^1 = \frac{12(x_0 - x_f) + 6(x_0' + x_f')\tau_f + (x_0'' - x_f'')\tau_f^2}{24\pi}. \end{aligned} \tag{51}$$

The only problem is that the derivatives in Eqs.(51) are taken in the virtual domain, while the actual boundary conditions are given in the physical domain. Mapping between the virtual domain $[0;\tau_f]$ and physical domain $[0;t_f]$ is addressed by introducing a speed factor λ:

$$\lambda = \frac{d\tau}{dt}\,, \tag{52}$$

Using this speed factor we may now compute corresponding derivatives in the virtual domain using the obvious differentiation rules valid for any time-variant parameter ξ:

$$\dot{\xi} = \lambda \xi' \,,\ \ddot{\xi} = \lambda\left(\lambda' \xi' + \lambda \xi''\right). \tag{53}$$

Inverting Eqs.(53) yield:

$$\xi' = \lambda^{-1}\dot{\xi} \,,\ \xi'' = \lambda^{-2}\ddot{\xi} - \lambda'\lambda^{-1}\dot{\xi} \,. \tag{54}$$

Note that we only need to use Eqs.(54) once to transfer the boundary conditions. Since the speed factor λ simply scales the entire problem – the higher speed factor λ is, the larger τ_f it results in (see explanation in Ref.37) – we may let

$$\lambda_{0;f} = 1 \text{ and } \lambda'_{0;f} = 0 \,, \tag{55}$$

which means we can safely assume

$$\xi' = \dot{\xi} \,,\ \xi'' = \ddot{\xi} \,. \tag{56}$$

Now let us describe the numerical procedure for finding the optimal solution among all candidate trajectories described by Eqs.(46). First, we guess the value of the only varied parameter τ_f and compute the coefficients of the candidate trajectory using Eqs.(51) with the boundary conditions (47) and (48) converted to the virtual domain via Eqs.(54) (accounting for Eqs.(55)). For the initial value of τ_f we can take the length of the circumference connecting terminal points:

$$\tau_f = \frac{\pi}{2}\sqrt{(x_f - x_0)^2 + (y_f - y_0)^2} \,. \tag{57}$$

Having an analytical representation of the candidate trajectory, Eqs.(46) and (49), define the values of x_j, y_j, x'_j, and y'_j, $j = 1,...,N$ over a fixed set of N points spaced evenly along the virtual arc $[0;\tau_f]$ with the interval

$$\Delta\tau = \tau_f (N-1)^{-1} \,, \tag{58}$$

so that

$$\tau_j = \tau_{j-1} + \Delta\tau \,,\ j = 2,...,N \,,\ (\tau_1 = 0 \,). \tag{59}$$

Then, for each node $j = 2,...,N$ we compute

$$\Delta t_{j-1} = \sqrt{\frac{(x_j - x_{j-1})^2 + (y_j - y_{j-1})^2}{V_h^{*2} + W^2 - 2V_h^* W \cos\psi_{j-1}}} \tag{60}$$

($\psi_1 \equiv \psi_0$), and

$$\lambda_j = \Delta\tau \Delta t_{j-1}^{-1} \,. \tag{61}$$

The yaw angle ψ can now be computed using the virtual domain version of Eq.(43):

$$\psi_j = \tan^{-1}\frac{\lambda_j y'_j}{\lambda_j x'_j + W} \,. \tag{62}$$

Finally, the yaw rate $\dot{\psi}$ is evaluated using Eq.(44) (with time derivatives evaluated using Eq.(53)) or simply as

$$\dot{\psi}_j = (\psi_j - \psi_{j-1})\Delta t_{j-1}^{-1} \,. \tag{63}$$

When all parameters (states and controls) are computed in each of the N points, we can compute the performance index

$$J = \left(\sum_{j=1}^{N-1}\Delta t_j - T_{turn}\right)^2 + k^{\dot{\psi}}\Delta \,, \tag{64}$$

where

$$\Delta = \max_j\left(0;\left|\dot{\psi}_j\right| - \dot{\psi}_{j\max}\right)^2 \tag{65}$$

with $k^{\dot{\psi}}$ being a scaling (weighting) coefficient. Now the problem can be solved say in the Mathworks' development environment with as simple built-in optimization function as *fminbnd*. It should be noted that the numerical algorithm based on the direct method introduced in this section with the non-gradient optimization routine *fminbnd* based on the straight forward golden section search and parabolic interpolation algorithm allows computing the optimal turn trajectory very fast. To be more specific a 16bit 80MHz processor, allowed computation of the 17.5

second turn maneuver with $N = 20$ in 10 iterations, which took only 0.07s all together. With the controls update rate of 0.25s that means that the trajectory can be updated as often as every control cycle.

As a demonstration of the proposed approach, Fig.6 shows an example of the optimal final turn trajectory, which is essentially the same as in Fig.4b. However, as opposed to Fig.4b the yaw angle changes smoothly at departure from TIP and arrival to the top of the final approach. As a result the turn trajectory is slightly different from that of Fig.4b, but what is of the most importance is that ADS captures the final approach glide slope in exactly T_{turn} seconds as Fig.4b trajectory does.

Therefore, now we have a tool allowing us to construct the optimal trajectory from any initial point to the predetermined final point to be achieved in a certain time. To this end, even if we get to the TIP with errors as shown in Fig.4a, we can easily accommodate these errors and provide the optimal control so that we will still be at the top of the final approach in the predetermined time, T_{turn} (see Fig.7).

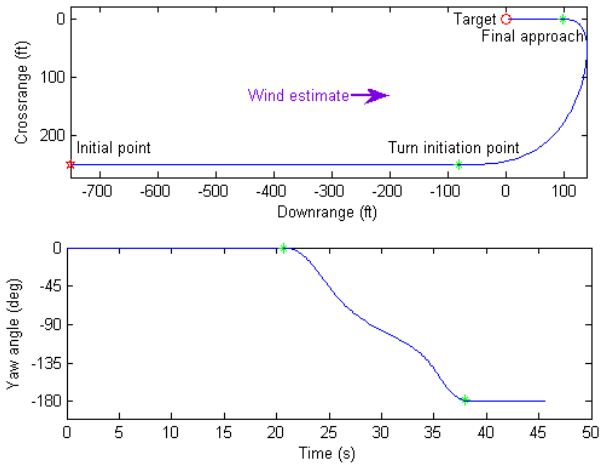

Fig.6 Optimal guidance in the perfect conditions as in Fig.4b.

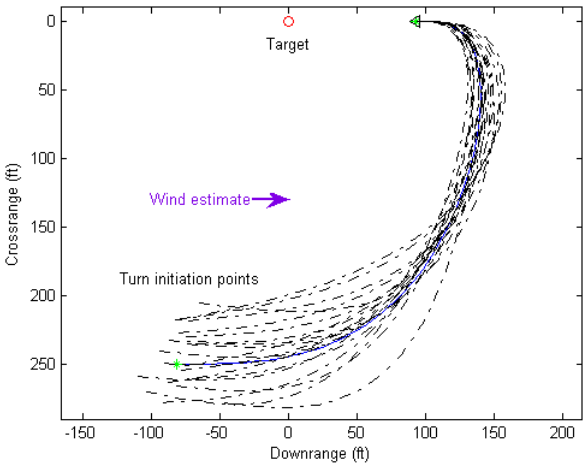

Fig.7 Optimal guidance with an error at TIP.

Similarly, in case of wind disturbances (Fig.5b) the ability to recompute the trajectory from the current (off the original trajectory) conditions to the same final conditions as often as practical seems to alleviate the problem. To this end, Fig.8 presents two examples of handling wind disturbances with the trajectory update rate set as a function of tracking error. Once the tracking error while following the previously generated trajectory exceeds a certain amount (10ft and 15ft in Fig.8a and 8b, respectfully) a new trajectory is being generated. In Fig.8 multiple reference trajectories are shown with the solid lines, while a continuous parafoil trajectory is shown with a dashed line. The points where the old reference trajectory was abandoned are depicted with the circles, and the corresponding locations of the parafoil blown away from the reference trajectory by strong (up to 15% of the forward speed) unaccounted winds is marked with triangles. In practice, the accuracy of a GPS sensor is on the order of 10ft, so rather than making trajectory updates according to a sliding error as shown in Fig.8, it is also possible to time schedule updates.

Although the optimal terminal guidance algorithm works well, several further adjustments need to be made in order to make it more robust in practice. The kinematic models in Eq.(42) does not account for parafoil turning dynamics and assumes that the sideslip and roll angles are small. When the turn rate is sufficiently small or the radius R is large, the model in Eq.(42) provides sufficient accuracy. However, in order to track the desired trajectory for a wide range of R, the error from sideslip and turning dynamics can be compensated by adding an additional commanded ψ for the first t_{pre} seconds after the TIP has been reached. Specifically, for the first t_{pre} seconds of the maneuver the command yaw rate ψ^c produced by Eq.(62) is augmented as follows:

$$\tilde{\psi}^c = \psi^c - K_{turn} \frac{V_h^*}{R} \tag{66}$$

where K_{turn} is the correction gain and V_h^* / R is the required constant turn rate in (33).

Disturbances from wind and sensor errors during tracking of the optimal trajectory will result in errors in final approach arrival. These errors can be accommodated by re-computing the optimal trajectory from the current (off the original trajectory) conditions to the desired final approach point during Phase 5. Re-computation of the optimal

trajectory is scheduled so that the specified number of updates occurs at equal intervals over the period from t_0 to t_{exit}.

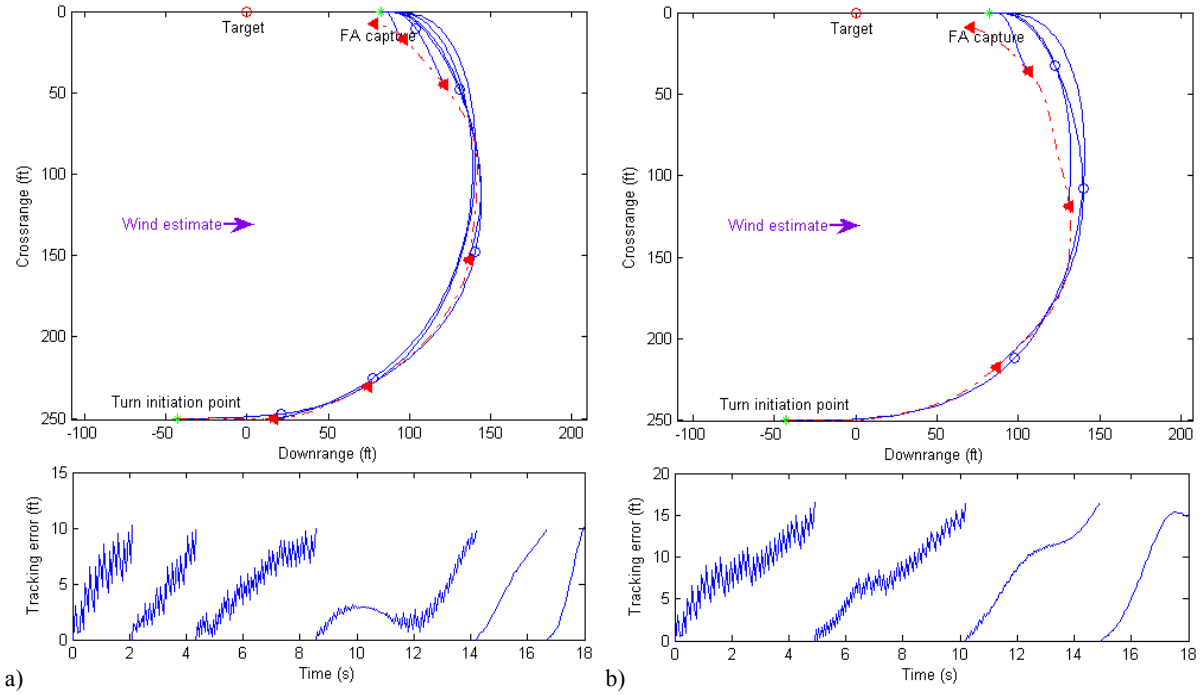

Fig.8 Optimal guidance with wind disturbance with a 10ft (a) and 15ft (b) cap on a tracking error.

The final capture location x_f (x at t_f in Eq.(48)) assumes that during phase 6 the parafoil travels directly to the target by the shortest path. In practice disturbances result in deviation from the shortest path and the guidance algorithm will result in a trajectory with less than perfect efficiency at reaching the target. In order to correct for realistic errors during the final approach the final capture location x_f is corrected to be

$$x_f = V_h^* T_{app}^{des} \varepsilon_{final} \tag{67}$$

where ε_{final} is the final approach efficiency.

Figures 9 and 10 show examples of how these additions to the guidance law work for desired turn radii of 125ft and 325ft, respectively. In Figs. 9 and 10 the full nonlinear parafoil model is simulated with the MPC control algorithm described previously used to track the desired ψ angle. In both cases T_{app} is 7.5s, ε_{final} is 0.95, t_1–t_{exit} is 3.0s, t_{pre} is 6.0s, K_{turn} is 1.0, V_h^* is 22.4ft/s, x_f is 88.4ft, and the wind W is -10ft/s. Results are shown from the TIP (x_0, y_0, z_0) for both cases which are (−88.3ft, 250ft, −311ft) for Fig.9 and (−363ft, 650ft, −658ft) for Fig.10. As seen, even with a single trajectory update (Fig.9a) the parafoil lands near desired location while additional updates allow for more correction near the end of the trajectory (Fig.9b). In Fig.10 the longer turn allows more error to accumulate with even one trajectory update resulting in a sufficient correction.

VII. Precision Placement Results

The complete precision placement algorithm is developed by combining the loitering pattern (Phases 1 and 2), exit decision (Phase 3) based on terminal guidance geometry, estimation of TIP (Phase 4), and the optimal terminal guidance and the final approach (Phases 5 and 6). The parafoil loiters in Phase 2 continuously estimating wind $\hat{W}$, air speed $\hat{V}_h^*$, and descent rate $\hat{V}_v^*$. The altitude at which to exit loitering and start towards the target z_{start} , found by using Eq.(39) assumes that the parafoil is already traveling towards the target. While loitering in Phase 2 there will be a delay between reaching the altitude z_{start} and when the parafoil can turn to face the target. In order achieve the desired final approach time T_{app}^{des} , the parafoil must exit loitering T_{delay} seconds early. The altitude to exit loitering can then be estimated by using Eq.(39) using the combined time $T_{delay} + T_{app}^{des}$ rather than the ideal T_{app}^{des} . Upon

exiting the loiter area Phase 4 is entered and the parafoil travels toward the target updating estimates of $\hat{D}_{switch}$. The location where the parafoil reaches $\hat{D}_{switch}$ is defined as the TIP and the beginning of Phase 5. After exiting the loiter pattern the approach time T_{app} is determined by Eq.(36). Due to disturbances, measurement error, and tracking error T_{app} may not match T_{app}^{des}. The optimal final trajectory is determined using the last estimates of $\hat{W}$, $\hat{V}_h^*$, $\hat{V}_v^*$ and T_{app} as outline in Section IV. While in Phase 5 the optimal final turn trajectory is continually updated until time t_{exit}, after which Phase 6 begins the final approach.

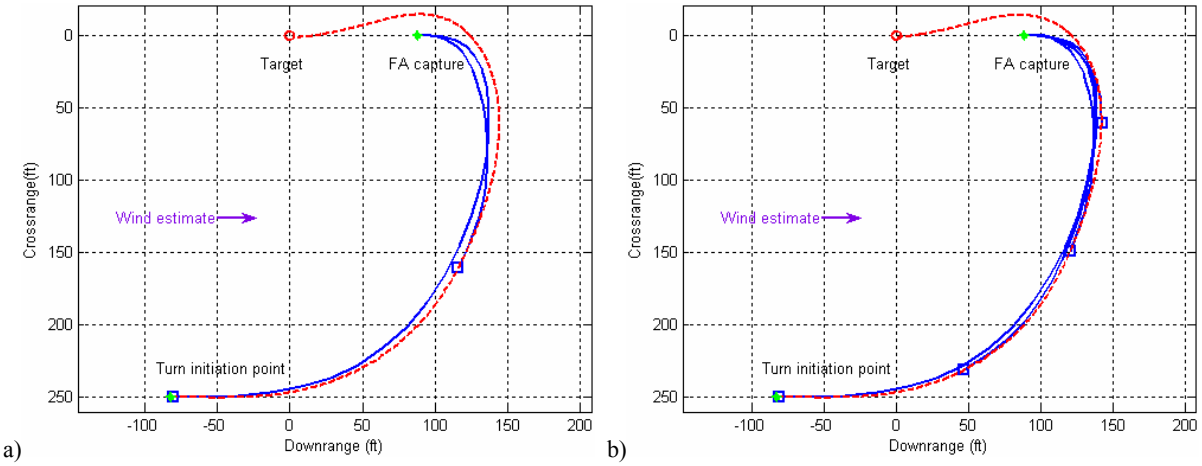

Fig.9 Optimal real-dynamics-augmented guidance with one (a) and three (b) trajectory updates with a 125ft turn radius.

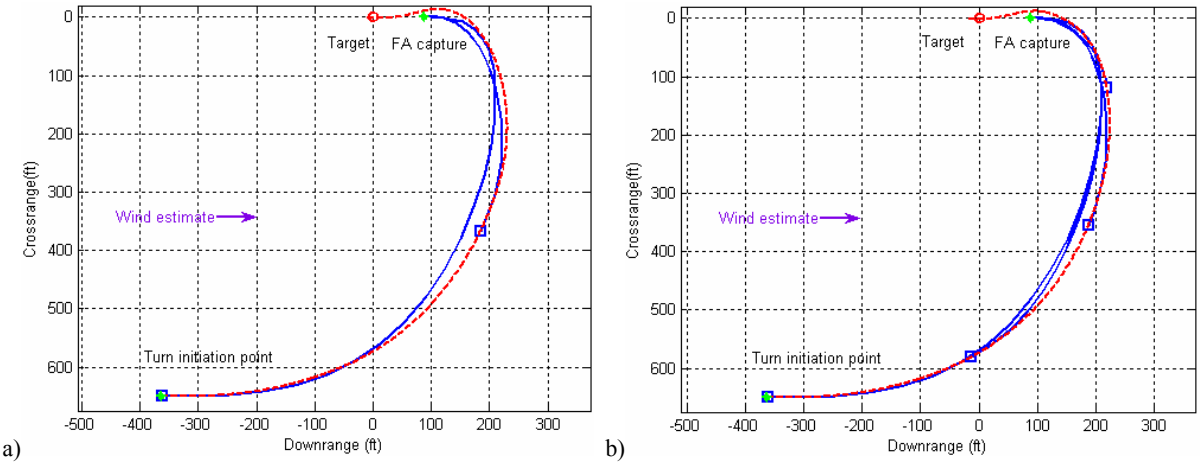

Fig.10 Optimal real-dynamics-augmented guidance with one (a) and three (b) trajectory updates with a 325ft turn radius.

The full algorithm is demonstrated through numerical integration of the nonlinear model starting from (x,y,z) of (−1200ft, −200ft, −2200ft). All precision placement parameters used are provided in Table 2. Winds are 10ft/s downrange (W = −10ft/s) both at altitude and ground level. During the final turn in Phase 5 two updates of the optimal trajectory are used. In all phases of guidance the MPC algorithm based on the linear parafoil approximation is used to track the desired ψ angle.

Results of the algorithm are shown in Figs. 11 to 13. Progression of algorithm phases is shown by triangles representing the transition to the next guidance phase, with the first transition marking the beginning of Phase 2. The trajectory is shown in Fig.11 with the four loiter region points marked by x's, optimal trajectory updates marked by squares, and the final target by a circle. Upon entering Phase 2 the parafoil circles the loiter region in a clockwise direction.

Table 2. Parameters of the precision placement algorithm.

Parameter	Value
Away distance	750 ft
Cycle distance	400 ft
Final turn radius, R	125 ft
T_{app}^{des}	7.5 s
T_{delay}	6.5 s
$k^{\dot{\psi}}$	400
$\dot{\psi}_{j\max}$	20 °/s
t_{pre}	6.0 s
t_1 - t_{exit}	3.0 s
ε_{final}	0.95
K_{turn}	1.0

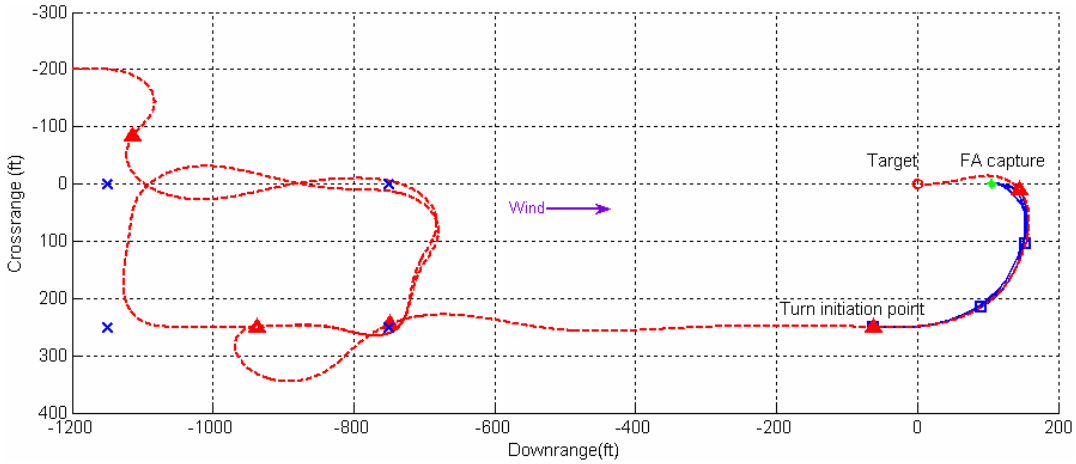

Fig.11 Precision placement trajectory.

Figure 12 shows the estimation of the exit altitude z_{start} from Eq.(39) based on current wind estimates, the approach time T_{app}^{des}, and transition delay T_{delay}. Transition from Phase 2 to 3 occurs when the altitude reaches z_{start} at 120 seconds at an altitude of 732ft. Figure 13 shows that T_{app} is 14.0s ($T_{app}^{des} + T_{delay}$) when Phase 3 is entered. Transition to Phase 4 occurs at 133s at which time T_{app} has decreased to 6.9 seconds due to the time required to make the turn exiting the loitering region. During Phase 4 it can be seen that the required T_{app} continues to vary as tracking error and wind estimates change. In Phase 4 the transition to the final turn occurs when $\hat{D}_{switch}$, the estimated distance to pass the target, is reached. Figure 12 shows $-\hat{D}_{switch}$, where the value is positive when the parafoil must turn before reaching the target and negative if the turn is to occur after passing the target. Early in the trajectory $-\hat{D}_{switch}$ is much less than zero demonstrating if a turn to target was performed at that time the parafoil would need to pass the target by a large amount before turning because of it current altitude. Transition from Phase 4 to 5 occurs when the distance to target L reaches $-\hat{D}_{switch}$ at 154 seconds with the parafoil 62ft ahead of the target. Two updates of the optimal final turn trajectory occur before transition to Phase 6 at 169 seconds. Final impact occurs at 2ft cross range and 8ft down range at 180.0 seconds.

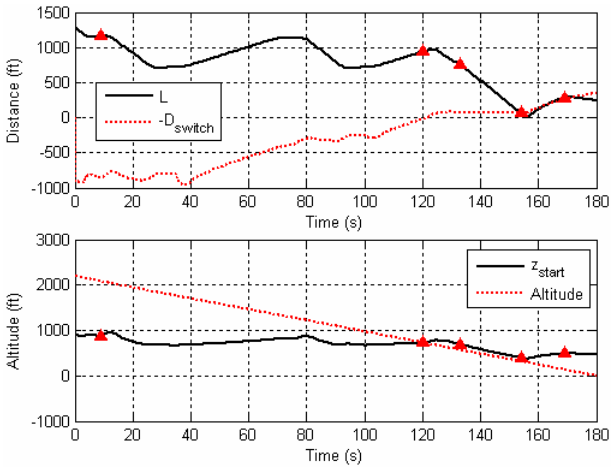

Fig.12 Terminal guidance decision variables.

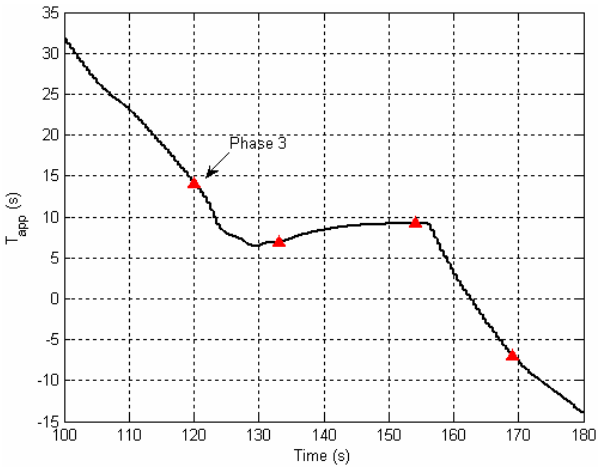

Fig.13 Final approach time.

Monte Carlo simulations of 50 drops were completed using the complete precision placement algorithm. Gaussian noise was injected into measured position, altitude, and inertial sensors. In addition to sensor errors, two sources of wind variation were added to the simulation; varying direction and varying ground wind magnitude. Wind was assumed to have a constant magnitude prior to terminal guidance. Wind magnitude varied linearly from W at the TIP altitude to W_F at the ground. Prevailing wind was assumed by the system to travel down range at a heading of zero degrees while the true wind varied in its direction. For all simulations, the target was set as the origin. Sensor noise and wind variation statistics are listed in Table 3. Dispersion results are shown in Fig.14. The resulting CEP is 55.1ft shown by the circle and is defined by the radius which includes 50 percent of the impacts. The results of real drops made at Camp Roberts, CA and Yuma Proving Ground, Yuma, AZ in the course of 2008 are discussed in Ref.38.

Table 3. Error statistics.

Parameter	Mean	Standard deviation
Initial position x	-1500 ft	250 ft
Initial position y	0 ft	250 ft
Initial position z	-3000 ft	250 ft
GPS x bias	0.0 ft	2.0 ft
GPS y bias	0.0 ft	2.0 ft
GPS x deviation	1.5 ft	0.0 ft
GPS y deviation	1.5 ft	0.0 ft
Altitude bias	0.0 ft	7.5 ft
Altitude variation	1.5 ft	0.0 ft
Roll, pitch and yaw bias	0.0 deg	2.0 deg
Roll, pitch and yaw deviation	1.0 deg	0.0 deg
u, v and w bias	0.0 ft/s	0.25 ft/s
u, v and w deviation	0.5 ft/s	0.0 ft/s
p, q, and r bias	0.0 deg	1.0 deg
p, q, and r deviation	1.0 deg	0.0 deg
W	-10.0 ft/s	3.3 ft/s
W_F	-10.0 ft/s	3.3 ft/s
Wind heading error	0.0 deg	15.0 deg

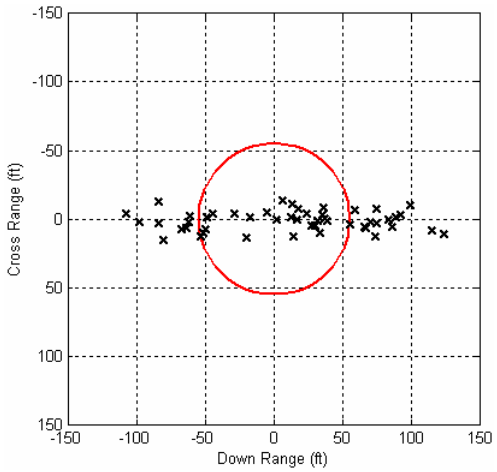

Fig.14 Monte Carlo simulation dispersion.

VIII. Conclusion

Using a simple kinematics model, an algorithm was developed allowing an aerial delivery system to predict a when to exit its loitering pattern. The algorithm allowed the system, in the presence of winds, to approach the target at an altitude, so that a final turn could be completed with the target being reached when impacting the ground. Uncertainty in winds, sensors, and guidance resulted in the system arriving only approximately at the predicted final approach location. In order to improve accuracy, a final turn reference trajectory based on the inverse dynamics in the virtual domain was generated. The method efficiently computes a reference trajectory solution to the two-point boundary-value problem using the current state of the aerial delivery system. Efficient computation allowed the trajectory to be recomputed during the final turn adding robustness to changing winds and tracking errors. The complete precision placement algorithm including; trajectory tracking, loiter exit decision, and final turn, was demonstrated through Monte Carlo simulations. The resulting algorithm had a circular error probable of 55.1ft for the example aerial delivery system.

Appendix: Model Parameters

System mass m, *slug*:			0.162		
Steady state aerodynamic velocity V_a, *ft/s*:			24.0		
Canopy reference area S_p, ft^2:			11.0		
Canopy span b, *ft*:			4.45		
Canopy chord $\bar{c}$, *ft*:			2.47		
Incidence angle Γ, deg.:			−12		
Inertia matrix elements, slug·m^2:			I_{xx} =0.312,	I_{yy} =0.296,	I_{zz} =0.039, I_{xz} =0.022
Elements of the apparent mass matrix $\mathbf{I}_{a.m.}$, *slug*:			A =0.008,	B =0.0022,	C =0.029
Elements of the apparent inertia matrix $\mathbf{I}_{a.i.}$, *slug*·m^2:			P =0.04,	Q =0.10,	R =0.0018
x-distance from mass center to apparent mass center x_{BM}, *ft*:			0.15		
z-distance from mass center to apparent mass center z_{BM}, *ft*:			−3.64		
Maximum brake deflection $\bar{d}$, *in*:			5		
Aerodynamic coefficients:	C_{D0} =0.25,	$C_{D\alpha 2}$ =0.12,	$C_{Y\beta}$ =−0.23,	C_{L0} =0.091,	$C_{L\alpha}$ =0.90,
	C_{m0} =0.35,	$C_{m\alpha}$ =−0.72,	C_{mq} =−1.49,		
	$C_{l\beta}$ =−0.036,	C_{lp} =−0.84,	C_{lr} =−0.082,	$C_{l\delta a}$ =−0.0035,	
	$C_{n\beta}$ =−0.0015,	C_{np} =−0.082,	C_{nr} =-0.27,	$C_{n\delta a}$ =0.0115.	

References

[1] Joint U.S. Army / U.S Air Force Field Manual 5-430-00-2, FM 5-430-00-2/AFJPAM 32-8013, vol.II, 1994.

[2] Wailes, W., and Hairington, N., "The Guided Parafoil Airborne Delivery System Program", *Proceedings of the 13th AIAA Aerodynamic Decelerator Systems Technology Conference*, Clearwater Beach, FL, May 15-18, 1995.

[3] Patel, S., Hackett, N.R., and Jorgensen D.S., "Qualification of the Guided Parafoil Air Delivery System-Light (GPADS-Light)," *Proceedings of the 14th AIAA Aerodynamic Decelerator Systems Technology Conference*, San Francisco, CA, June 3-5, 1997.

[4] Wytlie, T., and Downs, P., "Precision Parafoil Recovery - Providing Flexibility for Battlefield UAV Systems?," *Proceedings of the 14th AIAA Aerodynamic Decelerator Systems Technology Conference*, San Francisco, CA, June 3-5, 1997.

[5] Wyllie, T., "Parachute Recovery for UAV Systems," *Aircraft Engineering and Aerospace Technology*, vol.73, no.6, 2001, pp.542-551.

[6] Brown, G., and Benney, R., "Precision Aerial Delivery Systems in a Tactical Environment," *Proceedings of the 18th AIAA Aerodynamic Decelerator Systems Technology Conference and Seminar*, Munich, Germany, May 23-26, 2005.

[7] Smith, J., Bennett, B., and Fox R., "Development of the NASA X-38 Parafoil Landing System," *Proceedings of the 3rd AIAA Workshop on Weakly Ionized Gases Workshop*, Norfolk, VA, November 1-5, 1999.

[8] Smith, B.A., "Large X-38 Parafoil Passes First Flight Test," *Aviation Week and Space Technology*, vol.152, no.5, 2000, pp.40-44.

[9] Smith, J., Witkowski, A., and Woodruff P., "Parafoil Recovery Subsystem for the Genesis Space Return Capsule," *Proceedings of the 16th AIAA Aerodynamic Decelerator Systems Technology* Conference, Boston, MA, May 21-24, 2001.

[10] Stein, J., Madsen, C., and Strahan, A., "An Overview of the Guided Parafoil System Derived from X-38 Experience," *Proceedings of the 18th AIAA Aerodynamic Decelerator Systems Technology Conference and Seminar*, Munich, Germany, May 23-26, 2005.

[11] Hewgley, C.W., and Yakimenko, O., "Precision Guided Airdrop for Vertical Replenishment of Naval Vessels," *Proceedings of the 20th AIAA Aerodynamic Decelerator Systems Technology Conference and Seminar*, Seattle, WA, May 4-7, 2009.

[12] Benney, R., McGrath, J., McHugh, J., Noetscher, G., Tavan, S., and Patel, S. "DOD JPADS Programs Overview and NATO Activities," *Proceedings of the 19th AIAA Aerodynamic Decelerator Systems Technology Conference and Seminar*, Williamsburg, VA, May 21-24, 2007.

[13] Wright, R., Benney, R., and McHugh, J., "Precision Airdrop System," *Proceedings of the 18th AIAA Aerodynamic Decelerator Systems Technology Conference and Seminar*, Munich, Germany, May 23-26, 2005.

[14] Wright, R., Benney, R., and McHugh, J., "An On-Board 4D Atmospheric Modeling System to Support Precision Airdrop," *Proccedings of Infotech@Aerospace*, Arlington, Virginia, Sep. 26-29, 2005.

[15] Cambell, D., Fill, T., Hattis, P., and Tavan, S., "An On-Board Mission Planning System to Facilitate Precision Airdrop," *Proceedings of Infotech@Aerospace*, Arlington, Virginia, Sep. 26-29, 2005.

[16] Dellicker, S., Benney, R., and Brown, G., "Guidance and Control for Flat-Circular Parachutes," *Journal of Aircraft*, vol.38, no.5, 2001, pp.809-817.

[17] Yakimenko O., Dobrokhodov V., and Kaminer I., "Synthesis of Optimal Control and Flight Testing of Autonomous Circular Parachute," *Journal of Guidance, Control, and Dynamics*, vol.27, no.1, 2004, pp.29-40.

[18] Jorgensen, D., and Hickey, M., "The AGAS 2000 Precision Airdrop System," *Proceedings of Infotech@Aerospace*, Arlington, Virginia, September 26-29, 2005.

[19] Gimadieva, T. Z., "Optimal Control of a Guiding Gliding Parachute System," *Journal of Mathematical Sciences*, vol.103, no.1, 2001, pp.54-60.

[20] Sim, A.G., Murray, J.E., Neufeld, D.C., and Reed, R.D., "Development and Flight Test of a Deployable Precision Landing System," *Journal of Aircraft*, vol.31, no.5, 1994, pp.1101-1108.

[21] Hattis, P.D., Polutchko, R.J., Appleby, B.D., Barrows, T.M., Fill, T.J., Kachmar, P.M., and McAteer, T.D., "Final Report: Development and Demonstration Test of a Ram-Air Parafoil Precision Guided Airdrop System," Volumes 1 through 4 (Report CSDL-R-2752, Oct. 1996) and Addendum (Report CSDL-R-2771, Dec. 1996), *Charles Stark Draper Laboratory*, Cambridge, MA

[22] Hattis, P.D., Appleby, B.D., and Fill, T.J., and Benney, R., "Precision Guided Airdrop System Flight Test Results," *Proceedings of the 14th AIAA Aerodynamic Decelerator Systems Technology Conference*, San Francisco, CA, June 3-5, 1997.

[23] Hattis, P., Campbell, D., Carter, D., McConley, M., and Tavan, S. "Providing Means for Precision Airdrop Delivery from High Altitude," *Proceedings of AIAA Guidance, Navigation, and Control Conference and Exhibit*, Keystone, Colorado, Aug. 21-24, 2006.

[24] Hattis, P., "Autonomous Large Parafoil Guidance, Navigation, and Control System Design Status," *Proceedings of the 19th AIAA Aerodynamic Decelerator Systems Technology Conference and Seminar*, Williamsburg, VA, May 21-24, 2007.

[25] Wegereef, J., Leiden, B.V., and Jentink, H., "Modular Approach of Precision Airdrop System SPADES," *Proceedings of the 19th AIAA Aerodynamic Decelerator Systems Technology Conference and Seminar*, Williamsburg, VA, May 21-24, 2007.

[26] Slegers, N., and Costello, M., "Aspects of Control for a Parafoil and Payload System," *Journal of Guidance, Control, and Dynamics*, vol.26, no.6, 2003, pp.898-905.

[27] Slegers, N., and Costello, M., "Model Predictive Control of a Parafoil and Payload System," *Journal of Guidance, Control, and Dynamics*, vol.28, no.4, 2005, pp.816-821.

[28] Slegers, N., Beyer, E., and Costello, M., "Use of Dynamic Incidence Angle for Glide Slope Control of Autonomous Parafoils," *Journal of Guidance, Control, and Dynamics*, vol.31, no.3, 2008, pp.585-596.

[29] Calise, A., and Preston, D., "Swarming/Flocking and Collision Avoidance for Mass Airdrop of Autonomous Guided Parafoils," *Proceedings of the AIAA Guidance, Navigation, and Control Conference and Exhibit*, San Francisco, California, Aug. 15-18, 2005.

[30] Calise, A., and Preston, D., "Design of a Stability Augmentation System for Airdrop of Autonomous Guided Parafoils," *Proceedings of the AIAA Guidance, Navigation, and Control Conference and Exhibit*, Keystone, Colorado, Aug. 21-24, 2006.

[31] Calise, A., Preston, D., and Ludwig, G., "Modeling for Guidance and Control Design of Autonomous Guided Parafoils," *Proceedings of the 19th AIAA Aerodynamic Decelerator Systems Technology Conference and Seminar*, Williamsburg, VA, May 21-24, 2007.

[32] Benney, R., Barber, J., McGrath, J., McHugh, J., Noetscher, G., and Tavan, S., "The Joint Precision Airdrop System Advanced Concept Technology Demonstration," *Proceedings of the 18th AIAA Aerodynamic Decelerator Systems Technology Conference and Seminar*, Munich, Germany, May 23-26, 2005.

[33] McHugh, J., Benney, R., and Miletti, J., and Mortaloni, P., U.S. Army Yuma Proving Ground, Yuma, AZ , "Planning, Execution and Results of the Precision Airdrop Technology Conference and Demonstration (2003)," *Proceedings of the 18th AIAA Aerodynamic Decelerator Systems Technology Conference and Seminar*, Munich, Germany, May 23-26, 2005.

[34] Delwarde, C., de Lassat de Pressigny, Y., Benney, R., Vallance, M., Norton, B., and Wintgens, J., "Precision Airdrop Capability Demonstration In France," *Proceedings of the 19th AIAA Aerodynamic Decelerator Systems Technology Conference and Seminar*, Williamsburg, VA, May 21-24, 2007.

[35] Lissaman, P., and Brown, G., "Apparent Mass Effects on Parafoil Dynamics," AIAA Paper 93-1236, May 1993.

[36] Yakimenko, O., "Direct Method for Rapid Prototyping of Near-Optimal Aircraft Trajectories," *AIAA Journal of Guidance, Control, and Dynamics,* vol.23, no.5, 2000, pp.865-875.

[37] Lukacs, J., and Yakimenko, O., "Trajectory-Shaping Guidance for Interception of Ballistic Missiles during the Boost Phase," *AIAA Journal of Guidance, Control, and Dynamics*, vol.31, no.5, 2008, pp.1524-1531.

[38] Yakimenko, O., Slegers, N., and Tiaden, R., "Development and Testing of the Miniature Aerial Delivery System Snowflake," *Proceedings of the 20th AIAA Aerodynamic Decelerator Systems Technology Conference and Seminar*, Seattle, WA, May 4-7, 2009.